Response of the middle atmosphere to anthropogenic and natural forcings in the CMIP5 simulations with the Max Planck Institute Earth system model

H. Schmidt,[1] S. Rast,[1] F. Bunzel,[1] M. Esch,[1] M. Giorgetta,[1] S. Kinne,[1] T. Krismer,[1] G. Stenchikov,[2] C. Timmreck,[1] L. Tomassini,[1] and M. Walz[3]

Received 1 August 2012; revised 29 October 2012; accepted 4 January 2013; published 6 March 2013.

[1] The ECHAM6 atmospheric general circulation model is the atmosphere component of the Max Planck Institute Earth System Model (MPI-ESM) that is used in the Coupled Model Intercomparison Project Phase 5 (CMIP5) simulations. As ECHAM6 has its uppermost layer centered at 0.01 hPa in the upper mesosphere, these simulations offer the opportunity to study the middle atmosphere climate change and its relation to the troposphere on the basis of a very comprehensive set of state-of-the-art model simulations. The goals of this paper are (a) to introduce those new features of ECHAM6 particularly relevant for the middle atmosphere, including external forcing data, and (b) to evaluate the simulated middle atmosphere and describe the simulated response to natural and anthropogenic forcings. New features in ECHAM6 with respect to ECHAM5 include a new short-wave radiation scheme, the option to vary spectral irradiance independent of total solar irradiance, and a latitude-dependent gravity-wave source strength. The description of external forcing data focuses on solar irradiance and ozone. Stratospheric temperature trends simulated with the MPI-ESM for the last decades of the 20th century agree well with observations. The future projections depend strongly on the scenario. Under the high emission scenario RCP8.5, simulated temperatures are locally lower by more than 20 K than preindustrial values. Many of the simulated patterns of the responses to natural forcings as provided by solar variability, volcanic aerosols, and El Niño–Southern Oscillation, largely agree with the observations.

Citation: Schmidt, H., S. Rast, F. Bunzel, M. Esch, M. Giorgetta, S. Kinne, T. Krismer, G. Stenchikov, C. Timmreck, L. Tomassini, and M. Walz (2013), Response of the middle atmosphere to anthropogenic and natural forcings in the CMIP5 simulations with the Max Planck Institute Earth system model, *J. Adv. Model. Earth Syst.*, *5*, 98–116, doi:10.1002/jame.20014.

1. Introduction

[2] The stratosphere and mesosphere, which cover the altitude range from about 10 to 100 km of the Earth's atmosphere, are often referred to as the middle atmosphere. It has been known for many decades that the middle atmosphere is strongly influenced by tropospheric weather and climate via upward propagating waves [e.g., *Andrews et al.*, 1987]. The stratosphere has received particular scientific attention since the discovery of the Antarctic ozone hole [*Farman et al.*, 1985] which affects the biosphere through the shielding effect of ozone on solar UV irradiance. For about a decade, there has been increasing evidence that the stratosphere influences the troposphere also via dynamical processes. *Baldwin and Dunkerton* [2001] have shown that anomalies of the northern hemisphere (NH) polar vortex may propagate downward from the stratosphere during winter and affect middle- and high-latitude surface weather patterns on a timescale of several weeks. *Thompson and Solomon* [2002] have shown that changes of the Antarctic polar vortex resulting from the development of the ozone hole have an influence on climate in high latitudes of the southern hemisphere (SH).

[3] An important challenge in contemporary climate research is to disentangle natural and anthropogenic sources of observed climate variations. In recent years many studies have suggested that the middle atmosphere plays an important role for the influence of natural forcings on climate. UV variability of solar irradiance influences stratospheric ozone, temperature, and dynamics, and these signals are thought to propagate downward to the troposphere via the polar vortices

[1]Atmosphere in the Earth System, Max Planck Institute for Meteorology, Hamburg, Germany.
[2]Physical Sciences and Engineering Division, King Abdullah University of Science and Technology, Thuwal, Saudi Arabia.
[3]Institute of Meteorology, Free University of Berlin, Berlin, Germany.

1942-2466/13/10.1002/jame.20014

but also via tropical pathways [e.g., *Gray et al*., 2010]. Similar effects have been identified for stratospheric sulfate aerosols resulting from large volcanic eruptions [e.g., *Robock*, 2000; *Timmreck*, 2012]. From observations and simulations it has also become clear that tropospheric tropical variability characterized by the El Niño–Southern Oscillation (ENSO) has an influence on the high-latitude stratospheric circulation, which may influence the troposphere [e.g., *Cagnazzo and Manzini*, 2009]. Furthermore, simulations presented by *Scaife et al*. [2005] indicate that the stratosphere plays a role in mediating climate change signals and that simulated regional patterns of tropospheric climate change depend on the vertical extension of the model, i.e., on the inclusion of a well-resolved stratosphere.

[4] The above mentioned gain of knowledge on the relevance of the middle atmosphere for the troposphere has prompted many weather and climate research centers to lift the upper lid of their respective models. This becomes evident in the context of the Coupled Model Intercomparison Project (CMIP). Most climate models participating in the previous intercomparison study (CMIP3) [*Meehl et al*., 2007] had their upper lid at altitudes close to about 10 hPa; about half of the models participating in the current CMIP5 activity [e.g., *Taylor et al*., 2012] have upper lids above 1 hPa, i.e., include at least a fully resolved stratosphere (see, e.g., E. Manzini et al., Role of the stratosphere in northern winter climate change as simulated by the CMIP5 models, submitted to *Journal of Geophysical Research*, 2012, hereinafter referred to as Manzini et al., submitted manuscript, 2012). This is true for the Max Planck Institute Earth System Model (MPI-ESM, M. A. Giorgetta et al., Climate change from 1850 to 2100 in MPI-ESM simulations for the Coupled Model Intercomparison Project 5, submitted to *Journal of Advances in Modeling Earth Systems*, 2012, hereinafter referred to as Giorgetta et al., submitted manuscript, 2012), the atmospheric component of which (ECHAM6) [*Stevens et al.*, 2013] has the uppermost layer centered at 0.01 hPa (approximately 80 km). While a similar configuration had already been developed for the predecessors ECHAM4 and ECHAM5 [*Manzini et al*., 1997, 2006], only now this vertically extended version has become the standard configuration and as such was used in all the CMIP5 simulations performed with the MPI-ESM.

[5] This paper describes those features of ECHAM6 most relevant for the middle atmosphere (section 2). This includes in particular the data sets used in the simulations to represent natural forcings from the Sun and volcanoes (sections 2.3 and 2.5, respectively). Furthermore, we will describe and evaluate basic features of the simulated middle atmosphere dynamics (section 3) and their response to anthropogenic (section 4) and natural (section 5) forcings. This paper should thereby serve, on the one hand, as a reference for subsequent more detailed studies of troposphere-stratosphere coupling and in particular for the use of MPI-ESM results in the model intercomparison studies. On the other hand, studies of the response of the middle atmosphere to natural and anthropogenic forcings with an ESM of such complexity in a large number of (mostly ensemble) experiments are only becoming possible now with the availability of the CMIP5 simulations, and the results presented here may improve our understanding of the middle atmosphere itself.

2. Description of Model, Numerical Experiments, and Natural Forcing Data

2.1. Features of ECHAM6 Relevant for the Middle Atmosphere

[6] ECHAM6 is an atmospheric general circulation model (GCM), with a mixed spectral-transform finite difference dynamical core, and serves as the atmospheric component in the MPI-ESM. Major characteristics of the full ESM and its performance in the CMIP5 experiments are described by Giorgetta et al. (submitted manuscript, 2012). The history of the ECHAM family of atmospheric GCMs, as well as a description of ECHAM6 and its performance in the CMIP5 experiments with a focus on the troposphere, is provided by *Stevens et al.* [2013]. The focus of our description is the gravity-wave parameterization because of its relevance for the circulation of the middle atmosphere and of some new tuning introduced in ECHAM6, and the parameterization of water vapor which is a new feature of ECHAM6. However, other model features that have been changed in the transition from ECHAM5 [*Roeckner et al*., 2006] to ECHAM6 can be expected to influence the middle atmosphere. This is particularly true for the treatment of solar radiative transfer. ECHAM5 used the model of *Fouquart and Bonnel* [1980] with four and, in later versions, six [*Cagnazzo et al*., 2007] spectral bands. This scheme has been replaced in ECHAM6 by the Rapid Radiative Transfer Model optimized for application in general circulation modeling (RRTM-G) approach [*Mlawer et al*., 1998; *Stevens et al.* 2013] which splits the solar spectrum into 14 bands and thereby better represents spectral variations in solar irradiance. The exact distribution of the 14 bands is described by S. Kinne et al. (A new global aerosol climatology for climate studies, submitted to *Journal of Advances in Modeling Earth Systems*, 2012, hereinafter referred to as Kinne et al., submitted manuscript, 2012).

[7] The CMIP5 simulations with the MPI-ESM have been performed mainly with two versions referred to as LR (low resolution) and MR (mixed resolution). These versions differ in the grids of the ocean (J. H. Jungclaus et al., Characteristics of the ocean simulations in MPIOM, the ocean component of MPI-Earth System Model, submitted to *Journal of Advances in Modeling Earth Systems*, 2012, hereinafter referred to as Jungclaus et al., submitted manuscript, 2012) and atmosphere components. The horizontal resolution of the atmospheric component is given in both versions by a triangular truncation at 63 wave numbers (T63). However, the vertical resolution differs between LR and MR. Although in both versions the uppermost layer is centered at 0.01 hPa, LR uses 47 and MR 95 vertical layers. The grids are called L47 and L95, respectively.

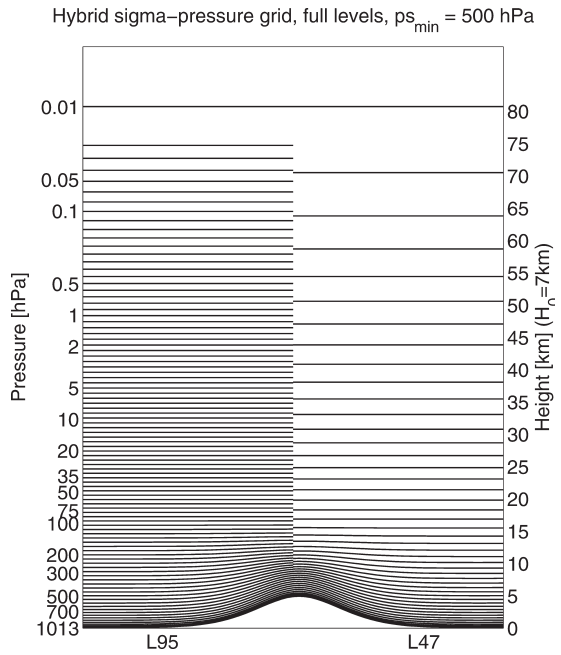

Figure 1. Spacing of the hybrid vertical layers in the (left) L95 (MR) and (right) L47 (LR) configurations of ECHAM6. Horizontal lines indicate the altitudes at the center of each layer for an assumed surface pressure of 500 hPa in the horizontal center of the plot and of 1013.25 hPa away from the center.

Figure 1 indicates the vertical distribution of the hybrid model layers for both configurations. In the lower and middle troposphere, the grids are identical. However, in the stratosphere, the vertical resolution is much finer (about 800 m) in L95 than in L47 (about 2–3 km). This allows for the vertical propagation of a spectrum of waves that drive momentum deposition in the middle atmosphere and associated circulations as the quasi-biennial oscillation (QBO) of equatorial stratospheric winds in the MR configuration (section 3).

2.1.1. Gravity Waves

[8] Subgrid-scale gravity waves are a key element for large-scale middle atmospheric dynamics, as their upward transfer of momentum contributes to the limitation of zonal jets and drives, to a large extent, the meridional circulation, in particular above the stratopause. Hence, their effects have to be parameterized in atmospheric GCMs. Orographic gravity-wave drag and surface blocking are parameterized following *Lott and Miller* [1997], as in ECHAM5 (see *Roeckner et al*. [2003] for a detailed description). However, some parameters of this parameterization have been adjusted for use in ECHAM6 during the general tuning process of the MPI-ESM [*Mauritsen et al*., 2012].

[9] The parameterization of effects of a spectrum of gravity waves from nonorographic sources is based on the Doppler spread theory of propagation and dissipation of such a spectrum as formulated by *Hines* [1997a, 1997b]. The same parameterization had already been implemented in the middle atmosphere versions of ECHAM4 and ECHAM5 [*Manzini et al*., 1997, 2006] and was described in detail by *Manzini and McFarlane* [1998] and *Roeckner et al*. [2003]. As in ECHAM5 the launching height of the parameterized gravity-wave sources is set to be at a model level of about 680 hPa, which is the 10th level above the surface in both L47 and L95. The source strength of the gravity-wave spectrum is characterized in the parameterization by the total root-mean-square gravity-wave spectrum. Although in ECHAM5 this value was set uniformly to 1.0 m/s, ECHAM6 allows the definition of a source strength that depends on latitude. While in the simulations with the LR version the same uniform source strength as in ECHAM5 was used, in the MR simulations, the value of 1.0 m/s was applied only poleward of 10° of both hemispheres, increased to 1.2 m/s in the tropical region from 5°S to 5°N, and linearly interpolated between 5° and 10°. The goal of this tuning was to simulate a QBO of realistic frequency.

[10] Recently, we have discovered a bug in the implementation of the nonorographic gravity-wave parameterization in ECHAM6 that has affected all the CMIP5 simulations with the MPI-ESM. This bug was introduced during the code optimization to increase the model's computational efficiency and was not present in earlier implementations of the same scheme in ECHAM5. In the parameterization, waves are launched in the troposphere isotropically in eight azimuthal directions. However, the bug affected the gravity-wave momentum deposition in four of these directions. The effects of this were tested through comparing the Atmospheric Model Intercomparison Project (AMIP) simulations with MPI-ESM-MR with and without the bug. The resulting differences in the annual mean zonal mean zonal winds are below 0.5 m/s everywhere in the middle- and high-latitude NH troposphere and stratosphere below 5 hPa. In the SH troposphere and stratosphere, however, differences are larger peaking at 1–2 m/s over a large altitude range at about 60°S. Considerably larger differences occur close to the model top. The simulated QBO period is shorter by about 2 months in the debugged version. Given the fairly small effect of the bug on the simulated atmospheric mean state, we expect only small effects of the bug on the model's response to natural and anthropogenic forcings as presented in the following sections.

2.1.2. Water Vapor in the Middle Atmosphere

[11] In the stratosphere and mesosphere, the major source of water vapor, besides transport from the troposphere, is oxidation of methane. ECHAM6 includes a submodel that parameterizes methane oxidation and photolysis of water vapor in order to describe the most important chemical source and sink. The formulation of the processes and their description follow the respective implementation in the Integrated Forecast System (IFS) of the European Centre for Medium-Range Weather Forecasts (ECMWF; see IFS documentation Cy36r1, part IV, chapter 9). The scheme adds the two tendency terms Q_{methox} and Q_{photo} to the prognostic equation for the grid-cell mean mass mixing ratio of water vapor $\overline{r}_v$.

Table 1. CMIP5 Simulations Performed With the MPI-ESM and Analyzed in This Study

Name	Period	Number of Realizations	Varied Forcings		
			GHG	Solar	Volcanic
piControl	1000 years	1	−	−	−
Historical	1850–2005	3	+	+	+
RCP2.6	2006–2100[a]	LR: 3; MR: 1	+	+	−
RCP4.5	2006–2100[a]	3	+	+	−
RCP8.5	2006–2100[a]	LR: 3; MR: 1	+	+	−
AMIP[b]	1979–2008	3	+	+	+

[a]With the LR model, one member of the RCP ensembles has been continued until 2300.
[b]Performed with ECHAM6 only, i.e., without ocean coupling.

[12] Q_{methox} describes the parameterization of methane oxidation and is defined as

$$Q_{\mathrm{methox}} = \frac{\left(r_{v,\mathrm{lim}} - \overline{r}_v\right)}{\tau_{\mathrm{methox}}}. \quad (1)$$

[13] $r_{v,\mathrm{lim}}$ is set to 4.25 ppm and hence is independent of the methane mixing ratio acting on radiation and potentially changing methane concentrations during climate simulations. τ_{methox} depends on pressure and is set to 100 days for levels with a pressure of less than 0.5 hPa, infinity for levels with a pressure larger than 100 hPa, and interpolated between these levels. This means that water vapor production from methane is strongest in the mesosphere and not considered in the troposphere.

[14] Q_{photo} describes the photolysis of water vapor and is defined as

$$Q_{\mathrm{photo}} = -\frac{\overline{r}_v}{\tau_{\mathrm{photo}}}. \quad (2)$$

[15] τ_{photo} is set to infinity for levels with a pressure larger than 0.2 hPa and is interpolated above this level so that it would reach a value of 3 days at 0.001 hPa. This definition ensures that the photolysis of water vapor contributes significantly to the water vapor budget only above about 0.1 hPa where τ_{photo} reaches the values of less than 100 days.

2.2. Numerical Experiments

[16] All the CMIP5 experiments performed with the MPI-ESM use model configurations with the center of the topmost level in the upper mesosphere at 0.01 hPa. Giorgetta et al. (submitted manuscript, 2012) provide a full list of the performed experiments. Table 1 lists those experiments used in this study. The naming of experiments used in this manuscript follows that of *Taylor et al.* [2012].

[17] In the use of forcing data we followed the CMIP5 protocol and recommendations as strictly as possible, although additional decisions had to be taken. This concerned in particular solar forcing, ozone, and volcanic aerosols, which are relevant for the stratosphere and are described in the following subsections. All experiments prescribe greenhouse gas (GHG) concentrations as valid for the troposphere uniformly in the entire atmosphere. This means that in the transient simulations the assumed stratospheric CO_2 concentrations precede the real atmospheric concentrations by a few years. Time-dependent CO_2 mixing ratios used in our simulations are shown in Figure 2. Radiative forcing of tropospheric aerosols is prescribed as presented by Kinne et al. (submitted manuscript, 2012).

2.3. Solar Irradiance

[18] Temporal variations of solar irradiance depend on the wavelength. In ECHAM5, however, only total solar irradiance (TSI) was allowed to vary, and the distribution onto the spectral bands was fixed. For the new 14-band RRTM radiation scheme implemented in ECHAM6, the incoming solar irradiance of each band can vary with time independently.

[19] For historic and future solar irradiance data, we follow as closely as possible the recommendations for CMIP5 provided by the Stratospheric Processes and their Role in Climate (SPARC)/Solar Influence for SPARC (SOLARIS) project. Historic data for the period 1850 until 2008 were reconstructed based on the observations and the proxy data by J. Lean (Naval Research Laboratory, Washington, DC). TSI variations were reconstructed as described by *Froehlich* [2004] based on the time series of sunspots and faculae. The spectral dependence of the solar irradiance and its variability was determined as described in detail by *Lean* [2000].

[20] For use in ECHAM6, the original data have been averaged over the wavelength bands of the RRTM code. As recommended by SPARC/SOLARIS, the original data have been multiplied by a factor of 0.9965. This was done in order to obtain a TSI close to 1361 W/m^2 as suggested by recent observations instead of about 1368 W/m^2 assumed earlier. The temporal resolution of the original data is annual until 1881 and monthly from 1882 on. For use in ECHAM6 the data are linearly interpolated in time. However, it should be kept in mind that short-period variability of solar irradiance used as input in the CMIP5 simulations is larger after than before 1882

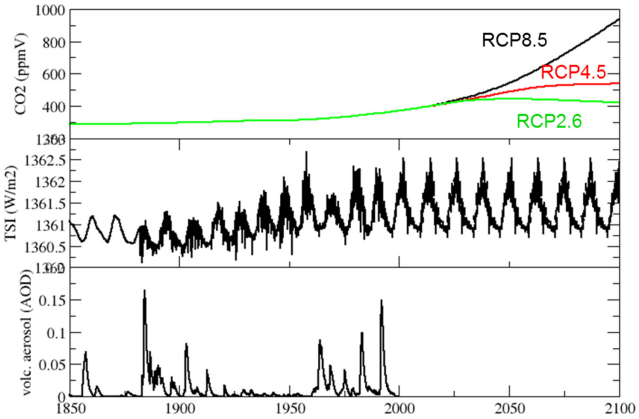

Figure 2. Monthly mean forcing data used in the CMIP5 simulations with the MPI-ESM for the period 1850–2100. (top) CO_2 volume mixing ratio (ppmV), (middle) TSI (W/m^2), and (bottom) vertically integrated globally AOD of volcanic aerosols.

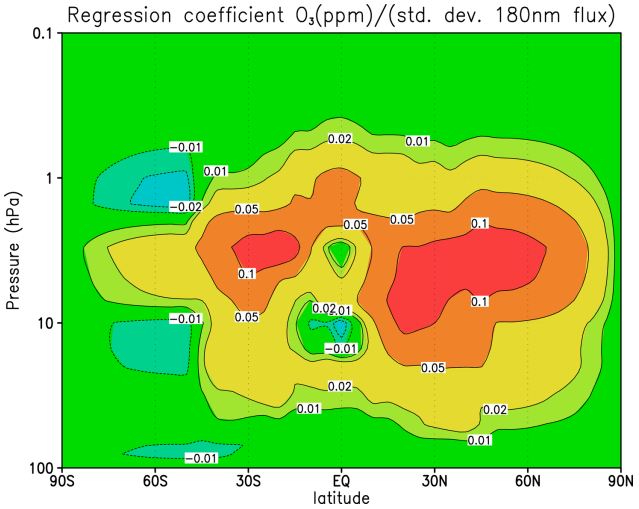

Figure 3. Regression coefficient used to parameterize the dependence of the zonal mean stratospheric ozone field on solar irradiance in ppmV per one standard deviation of the solar irradiance at 180.5 nm.

(see Figure 2). For the future scenarios we followed the recommendation to repeat solar cycle 23, i.e., irradiance data of the period May 1996 to July 2008 for August 2008 to October 2020, November 2020 to January 2033, etc. The time series of monthly TSI integrated from the spectral irradiances used for the period 1850–2100 is presented in Figure 2. For the preindustrial control simulation (piControl), constant irradiance, equal to the average value over the years 1844–1856, was used.

2.4. Ozone

[21] The data set for historic ozone concentrations was created within the projects Atmospheric Chemistry and Climate (AC&C) and SPARC for simulations (e.g., CMIP5) that do not take interactive chemistry into account [*Cionni et al.*, 2011]. The ozone data were prepared using satellite (SAGE I and II) and radiosonde data for the stratosphere, and model data (CAM3.5 and NASA-GISS PUCCINI) for the troposphere. These historic ozone data include the ozone reduction in the stratosphere caused by ozone depleting species and variations in ozone caused by solar variability. Ozone data are provided in terms of 3-D monthly averages. However, in the stratosphere the data set does not vary with longitude, so that only in the troposphere the real 3-D information is available.

[22] Original data exist only for altitudes with pressures larger than 1 hPa. Since the standard vertical resolutions include model layers with pressures as low as 0.01 hPa, the data set was extended upward by C. Bell (University of Reading, personal communication) applying the following formula:

$$O_3(z) = O_3(1\ \text{hPa}) \times \exp\frac{-(z - z(1\ \text{hPa}))}{H}, \quad (3)$$

with H set to 7 km and $O_3(z)$ denoting the mass mixing ratio of ozone at altitude z.

[23] Future ozone scenarios for the period 2008–2099 are provided from the same source mentioned for historic data. In the case of the future the data set is based on multimodel projections provided in the framework of the SPARC Chemistry-Climate Model Validation Activity [see *Cionni et al.*, 2011; *Eyring et al.*, 2010]. The original data set was extended upward as described above for the case of historical data. The original future ozone data set, however, does not include a solar cycle. In order to obtain the future ozone concentrations consistent with the assumptions for solar irradiance, a multilinear regression analysis was performed for the historical ozone data using solar irradiance at a wavelength of 180.5 nm and the stratospheric equivalent effective stratospheric chlorine content as regressors. The resulting regression coefficients for the ozone dependence on solar irradiance (see Figure 3) and the assumed future irradiance at 180.5 nm were then used to add a solar cycle dependence to the future stratospheric ozone. Tropospheric data (for $p \geq 100$ hPa) have not been modified, as the solar cycle dependence calculated from the historic data for this altitude regime is negligible. It should be noted that future ozone data sets depend on the representative concentration pathway (RCP) only in the troposphere. The simulations RCP2.6, RCP4.5, and RCP8.5 hence use the same stratospheric ozone data. The total column ozone for the three latitude bands for the years 1850–2099 is presented in Figure 4. It shows clearly the chlorine related decrease of total ozone since about 1970 and a recovery after about 2005. A solar cycle dependence is clearly visible for the tropical and northern high latitudes. At high southern latitudes the total ozone depends only weakly on solar variability.For the piControl simulation, constant monthly mean ozone fields averaged over the years 1850–1860 are used.

2.5. Volcanic Aerosols

[24] In the standard version of ECHAM6, aerosol optical properties are prescribed. Tropospheric natural and anthropogenic aerosol data used in the CMIP5 simulations with ECHAM6 are described by Kinne et al. (submitted manuscript, 2012). In the stratosphere,

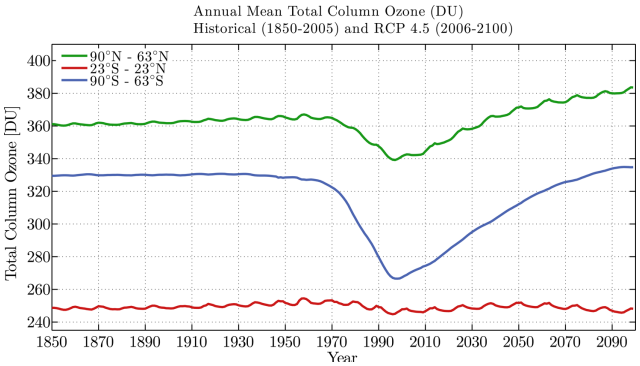

Figure 4. Time series of annual mean total column of ozone in Dobson units averaged over three latitude bands calculated from the ozone fields used as model input for the historical and RCP4.5 simulations.

background aerosols are ignored, and only sulfate aerosols resulting from volcanic eruptions are accounted for.

[25] The data set of volcanic forcing for the historic period from 1850 to 1999 is an extended version of the Pinatubo aerosol data set developed by *Stenchikov et al.* [1998] on the basis of satellite measurements of aerosol extinction and effective radii after the Pinatubo eruption and successfully applied in earlier model studies [*Stenchikov et al.*, 2004, 2006; *Thomas et al.*, 2009]. This data set contains monthly mean zonal averages of the aerosol extinction, the single scattering albedo, and the asymmetry factor as a function of time, pressure, and wavelength (i.e., the 30 spectral bands of the RRTM short- and long-wave codes used in ECHAM6). The data are given at 40 pressure levels and interpolated to the actual hybrid model layers during the simulations. For piControl and the years after 1999, zero stratospheric aerosols are assumed. The vertically integrated and globally averaged time series of monthly mean aerosol optical depth is presented in Figure 2.

3. Basic Characteristics of the Simulated Middle Atmosphere

3.1. Annual and DJF Averages

[26] In this section, zonal mean atmospheric parameters averaged over the years 1970–2000 of the three ensemble members of the historical simulation with the LR and MR configurations are presented as a reference for the responses to anthropogenic and natural forcings discussed in the following sections. Additionally, we compare the average fields to corresponding fields from the ECMWF ERA40 reanalysis (Figure 5). We concentrate on annual means and on averages over the NH winter months December, January, and February (DJF), which are of particular interest because of the relatively strong dynamical stratosphere-troposphere coupling during this period.

[27] The top two rows of Figure 6 show that annual mean temperature, zonal wind, and mass stream function of the LR and MR models. Differences between the two configurations are small except near to the upper lid and for the zonal wind in the tropics. Compared to ERA40 data (Figure 5 (top row)), simulated winds, temperature, and stream function show very similar structures. Tropopause temperatures are slightly underestimated in particular at high southern latitudes. Zonal mean zonal winds look very similar in ECHAM6 and ERA40 as well in terms of its pattern as of maximum velocities. There are large differences in variability between the LR and MR configurations in the tropics (bottom two rows of Figure 6). This is caused by the QBO being internally generated in the version with high vertical resolution (MR, see section 3.3). Therefore, the standard deviations of the MR configuration can be compared to ERA40. Furthermore, it should be noted that the observed standard deviation, in particular of ERA40 temperatures above 10 hPa, is strongly overestimated due to artificial jumps in the absolute temperatures introduced by the changes in the observation system. Below 10 hPa, the latitude and altitude dependence of standard deviations in both zonal wind and temperature are similar in ECHAM6-MR and ERA40. The QBO variability around 10 hPa is, however, overestimated by ECHAM6-MR. Standard deviations at polar latitudes are smaller than in ERA40.

[28] Figure 7 allows similar comparisons for DJF instead of annual averages. Again, differences between MR and LR in mean quantities are small except for the equatorial region. The westerly stratospheric jet is slightly stronger in MR than in LR. Comparison to ERA40 shows agreement in many features. The differences in interannual winter variability between LR and MR are again dominated by the QBO. However, the QBO seems to also cause a slightly increased variance of the NH stratospheric polar night jet. Compared to ERA40, the simulated interannual DJF variability, in particular of the polar night jet, seems well captured by the model (see also the following subsection). Interestingly, while the MR configuration seems to overestimate the QBO induced variability of tropical middle-stratospheric winds in the annual mean, the difference has the opposite sign for DJF means. This indicates different seasonalities of the simulated and real QBOs. The seasonality of the QBO simulated by ECHAM6 is discussed by T. R. Krismer et al. (Seasonal variability of the quasi biennial oscillation, submitted to *Journal of Advances in Modeling Earth Systems*, 2012, hereinafter referred to as Krismer et al., submitted manuscript, 2012).

3.2. Major Stratospheric Warmings

[29] Sudden stratospheric warmings are important manifestations of stratospheric winter variability but also interesting for potential downward coupling from the stratosphere to the troposphere [*Baldwin and Dunkerton*, 2001]. *Charlton and Polvani* [2007] and *Charlton et al.* [2007] have analyzed stratospheric warmings in reanalysis data and a variety of atmospheric GCMs. They defined major warmings as events where the polar night jet at 10 hPa and 60°N reverses its zonal direction and turns to easterly. They discarded such events that were not preceded by westerlies over at least 20 consecutive days and the final warmings that were identified when the jet did not return to westerlies for at least 10 consecutive days. In this study we follow the approach of *Charlton and Polvani* [2007] but use a minimum of 10 days instead of 20 days of westerlies to separate two events. In order to allow for proper statistics we have counted major warmings in the full historical ensembles. In LR and MR, major warmings occur with very similar frequency of 7.2 and 7.3 events/decade, respectively, compared to 6.0 and 6.4 events/decade counted by *Charlton and Polvani* [2007] in ERA40 and National Centers for Environmental Prediction/National Center for Atmospheric Research reanalysis data, respectively. The seasonal distribution from reanalysis data shows a convex distribution peaking in January, while the distribution simulated in the LR configuration is rather flat, and MR even shows a minimum in January (Figure 8). Already in the middle atmosphere version of ECHAM5

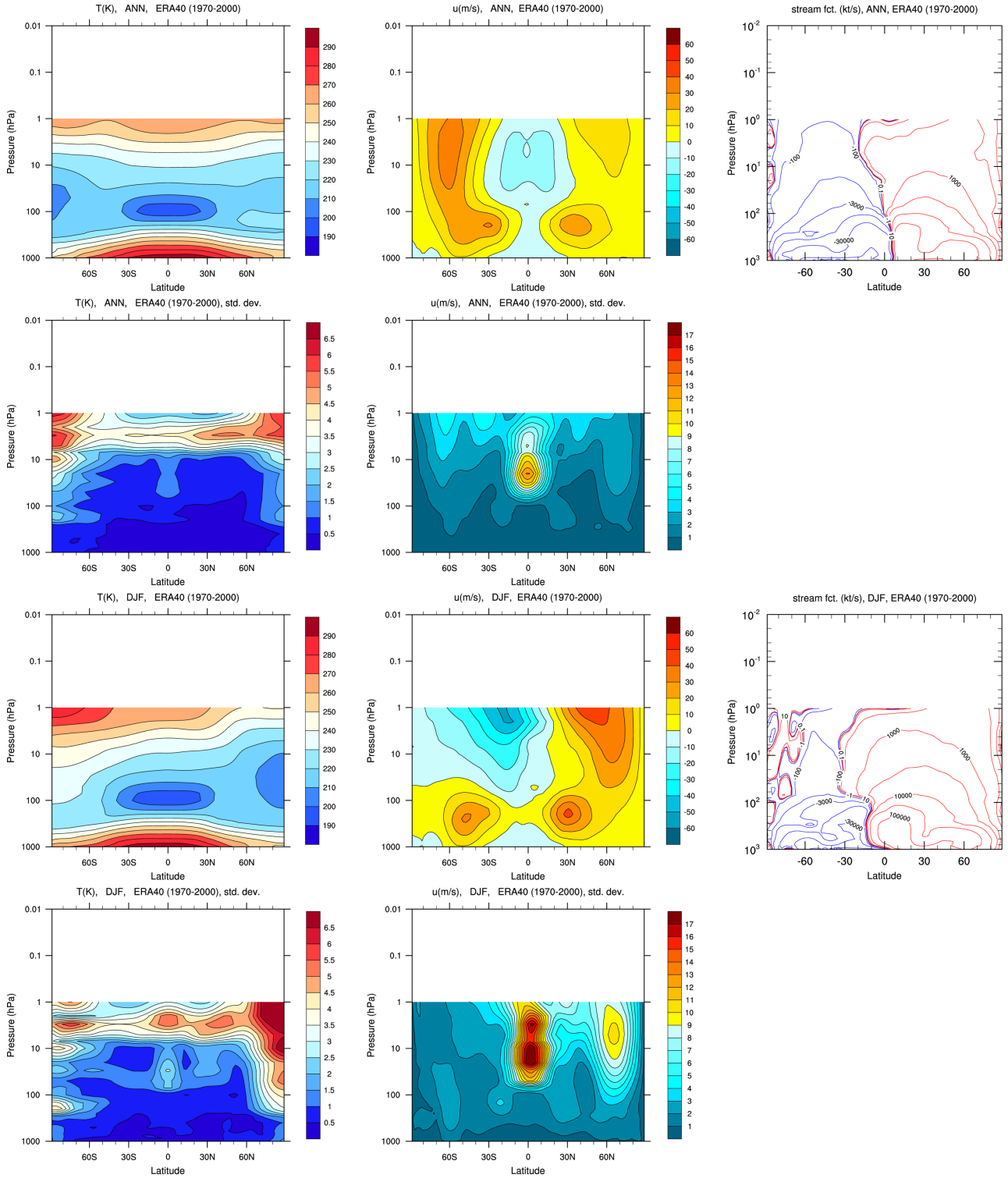

Figure 5. Zonal mean ERA40 reanalysis data averaged over the period 1970–2000. (left) Temperature (K), (center) zonal wind (m/s), and (right) mass stream function (kt/s). (top) Annual mean, (2nd row) standard deviation of annual mean, (3rd row) DJF mean, and (bottom) standard deviation of DJF mean.

(MAECHAM5), the observed seasonality of major warmings was not well reproduced, showing a maximum in November [*Charlton et al.*, 2007]. The simulated frequency was 5.2 events/decade. However, this analysis was based on only 29 years, simulated with an uncoupled model version at T42 horizontal resolution with 39 vertical layers. An MAECHAM5 simulation with T63 resolution and 47 vertical layers indicated a seasonal distribution closer to the observed one [*Bancalá et al.*, 2012].

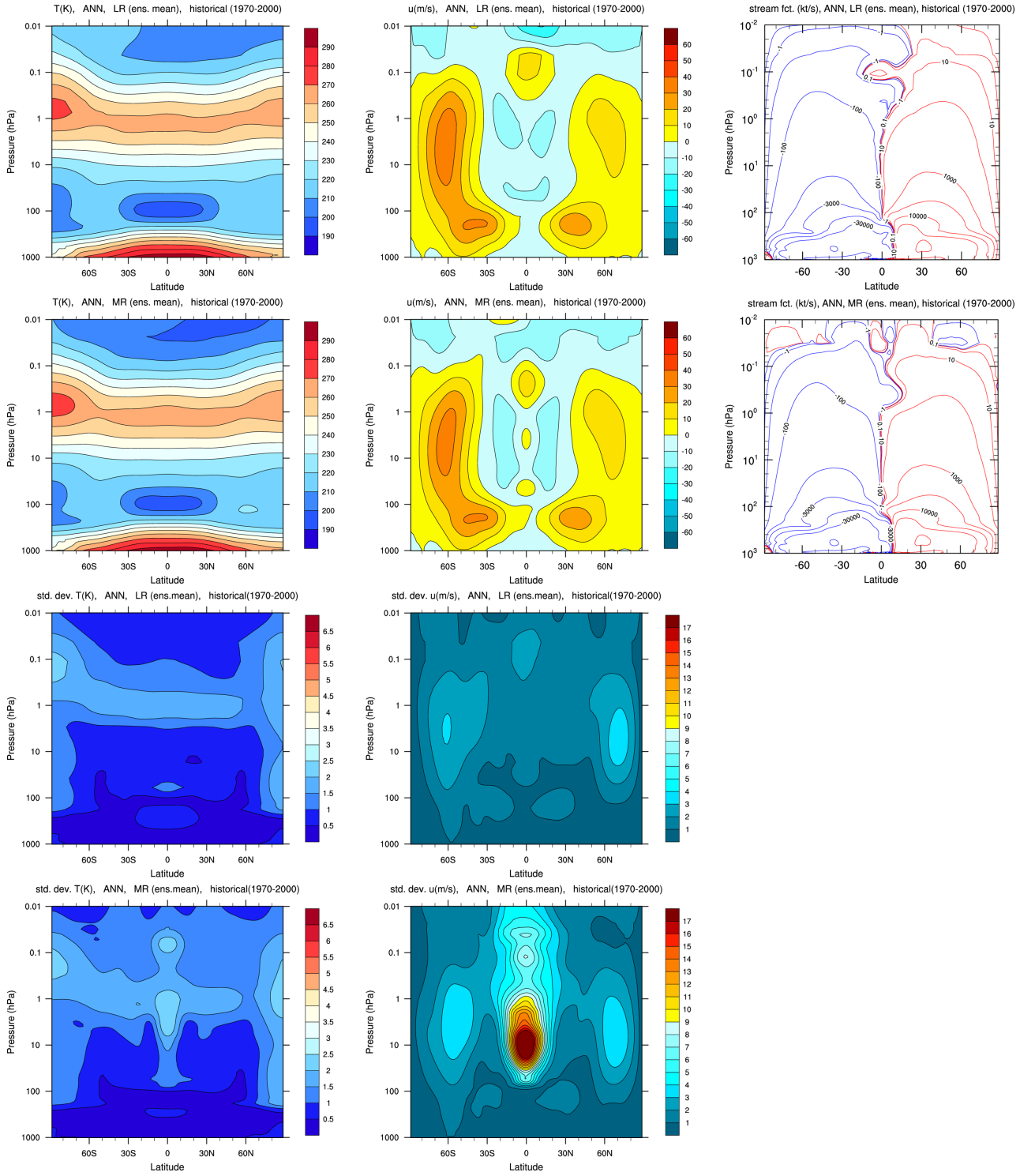

Figure 6. Annual and zonal mean values calculated from model results averaged over the years 1970–2000 of three realizations of the historical simulations. (left) Temperature (K), (center) zonal wind (m/s), and (right) stream function (kt/s). (top) MPI-ESM-LR, (2nd row) MPI-ESM-MR, (3rd row) standard deviation of annual means of MPI-ESM-LR, and (bottom) standard deviation of annual means of MPI-ESM-MR.

3.3. Quasi-Biennial Oscillation

[30] The QBO of equatorial stratospheric winds is thought to be caused by momentum deposition from a spectrum of upward propagating tropical waves including planetary and gravity waves [e.g., *Baldwin and Dunkerton*, 2001; *Giorgetta et al.*, 2002]. In the past decade, the QBO has been successfully produced internally in a few numerical models, among them MAECHAM5

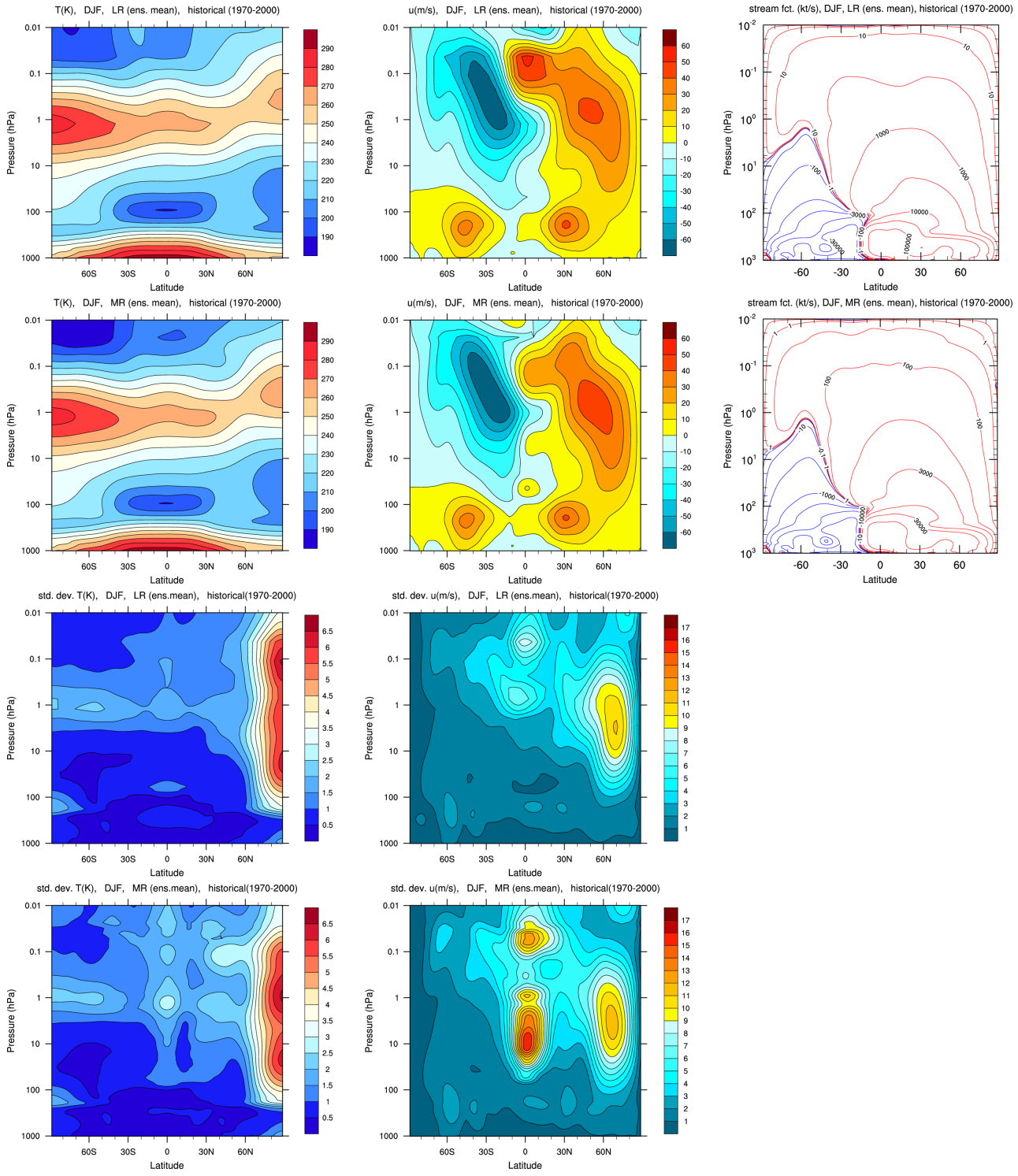

Figure 7. Same as Figure 6 but for NH winter months (DJF).

[*Giorgetta et al.*, 2006]. One prerequisite is a relatively high vertical resolution of, in general, less than 1 km. Figure 9 illustrates with two examples that the L95 version of ECHAM6 is also able to produce a QBO. For comparison, Figure 9 (bottom) shows the QBO in a simulation with the Hamburg Model of the Neutral and Ionized Atmosphere (HAMMONIA) [*Schmidt et al.*, 2006], an upward extension of MAECHAM5. In the specific simulation shown here, HAMMONIA was nudged to observations by radiosondes launched regularly from Singapore, and so the nudged HAMMONIA winds are taken as a proxy for the observed winds. In

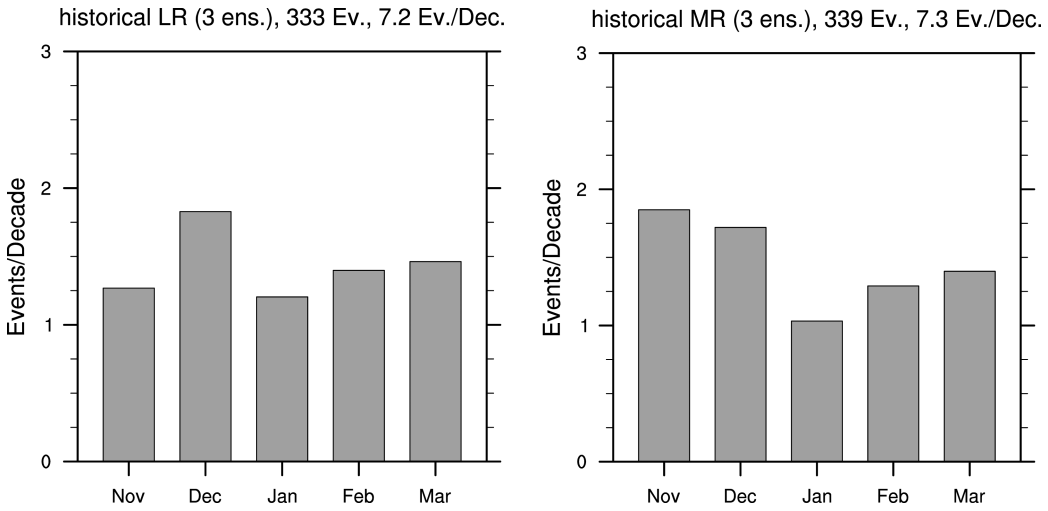

Figure 8. Occurrence frequency of sudden stratospheric warmings (see text for exact definition) averaged over the three realizations of the historical simulations with the (left) LR and (right) MR models.

the AMIP simulations (i.e., with prescribed sea surface temperatures (SSTs)), ECHAM6 simulates a slightly too short QBO period of about 26 months (compared to the observed period of about 28 months), but a too strong amplitude as was already indicated in the comparison of Figures 5 and 6. Also in the coupled historical simulations the amplitude is too strong. While at preindustrial times, the coupled model simulates a QBO of realistic 28 month period, the historical simulations show an increase of the length of the QBO period by about 3 months until 2000. To determine the origin of this trend in the QBO period is beyond the focus of this study. It is, however, consistent with the simulated strengthening in equatorial stratospheric upwelling (see following section) that has also been identified by *Kawatani et al*. [2012] as a reason for a GHG dependence of their simulated QBO period. Since the setting of the gravity-wave parameters is identical in both coupled and uncoupled model experiments, the differences in the QBOs simulated for the AMIP and historical simulations for the end of the 20th century (as shown in Figure 9) are likely caused by the influence of the SSTs. The coupled model has a cold bias in the SSTs of the tropical Pacific (Jungclaus et al., submitted manuscript, 2012) which may contribute to these differences.

4. Past and Future Trends

4.1. Temperature

[31] Balloon soundings provide fairly regular information on temperatures up to the middle stratosphere at selected locations since about the 1950s. With the satellite era, global temperature records have become available. However, offsets between instruments and the use of different techniques still impose challenges for the calculation of long-term trends. An analysis of data from satellites, radiosondes, and lidars by *Randel et al*. [2009a] indicates a cooling of about 0.5 K/decade in the low-latitude lower stratosphere and between about 0.5 and 1.5 K/decade in the middle and upper stratosphere for the period 1979–2007. Numerical simulations have indicated that the cooling is related to both the increase in CO_2 and the depletion of ozone [*Langematz et al*., 2003].

[32] Figure 10 shows the time series of tropical temperature simulated with the LR model for the period 1850–2100 at three different stratospheric pressure levels. Time series obtained with the MR model (not shown) looks very similar except for the higher variability from year to year and among ensemble members which is related to the QBO. At all altitudes trends are very weakly negative (on the order of -0.1 K/decade) between 1850 and about 1960. For the final three decades of the 20th century considerably accelerated temperature decreases of about -0.7, -0.5, and -1.7 K/decade at 47, 9, and 1 hPa, respectively, are simulated, which are of the same order as those calculated by *Randel et al*. [2009a]. Also, an ensemble average of several CMIP5 models shows good agreement with temperature trends observed in the recent past [*Charlton-Perez et al*., 2013]. The future evolution depends strongly on the scenario. In the lower stratosphere at 47 hPa the temperature continues to decrease in all scenarios. At the end of the 21st century, however the trend levels off for those scenarios in which the CO_2 mixing ratio stays constant (RCP4.5) or even starts to decrease (RCP2.6, cf. Figure 2). At 1 and 9 hPa RCP2.6 leads to clearly increasing temperatures after about the year 2040. In particular close to the stratopause, the radiative effect of ozone seems to play an important role as indicated by the slow temperature reduction after the decades of strong ozone depletion at the end of the 20th century. Under the high-emission scenario RCP8.5, the temperature in 2100 is projected to be about 18 K (at 1 hPa) and 12 K (at 9 hPa) lower than in 1850. Temperature differences between the extreme low and high emission scenarios in 2100 reach about 13 K at 1 hPa.

[33] Figure 11 provides information on temperature trends also for nontropical latitudes. As in all the

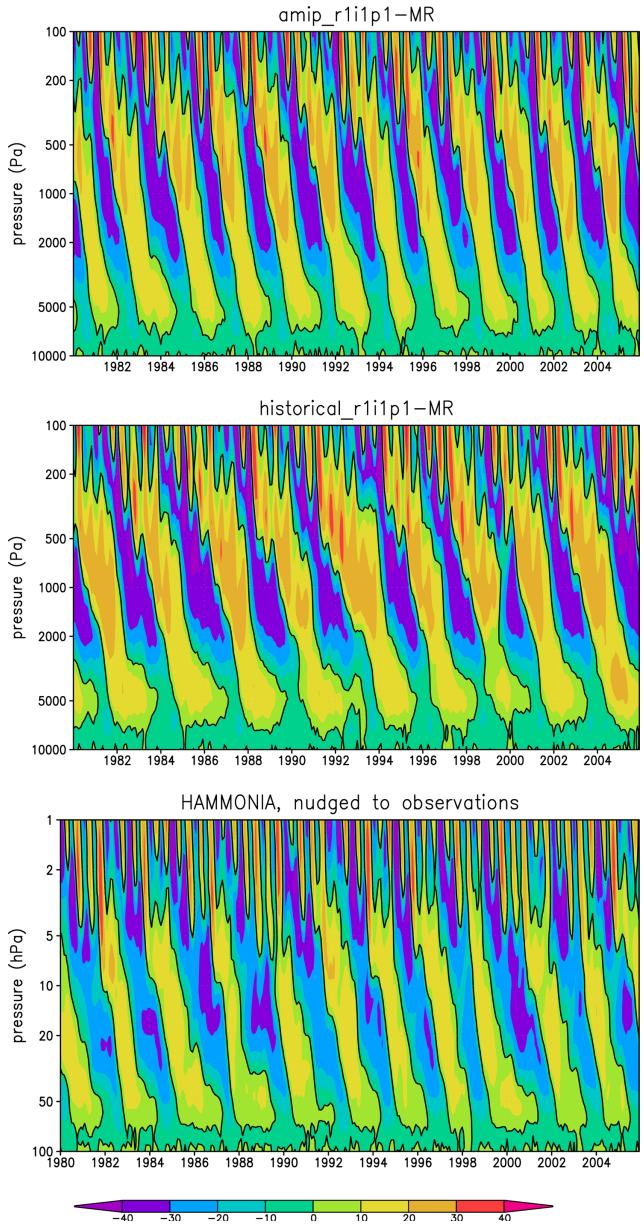

Figure 9. Twenty-six year periods of zonal mean zonal winds averaged over the equatorial region (5°S–5°N) from single realizations of three different simulations. (top–bottom) AMIP (ECHAM6-MR), historical (ECHAM6-MR), and HAMMONIA [*Schmidt et al.*, 2006] simulation nudged to observations from Singapore.

following discussions of trends we will concentrate on the LR simulation because the MR responses are in general very similar except for a more complicated structure in the equatorial region. The historical trend (comparison of the years 1970–2000 with the preindustrial state) as well as all scenarios (comparison of the years 2070–2100 with the years 1970–2000) show the expected distinct picture of tropospheric warming and middle atmospheric cooling. The maximum of the cooling, however, is located at different altitudes. In RCP2.6 it depends on the latitude and is located close to the tropical tropopause and close to about 7 hPa at middle and high latitudes. In RCP4.5 and RCP8.5 it is shifted upward toward the stratopause region at all latitudes. Also in the historical period the maximum is simulated close to 1 hPa but is peaking at low latitudes, while such a latitude dependence is not visible in the high emission RCPs.

[34] The only exception to the overall middle atmospheric cooling trend is the mesospheric region close to 0.1 hPa that responds to the small change of CO_2 in RCP2.6 by a very weak warming.

[35] Another particularity is the strong cooling in the lowermost SH tropopause in the historical ensemble that does not occur in any future scenario and is related to the development of the ozone hole at the end of the 20th century. In general, however, ozone depletion effects are smeared out by averaging over the years 1970–2000. The time series of Figure 10 points out the locally very strong trends during this period.

[36] Similar to annual means, also in the case of DJF trends (Figure 12), the maximum altitude of the cooling in the tropics and in the summer hemisphere depends on the scenario. However, DJF trends are much less symmetric about the equator. While the strongest cooling occurs between 10 and 1 hPa in the summer hemisphere it can be identified above 1 hPa in the winter hemisphere. This is related to the background temperature pattern (Figure 7) that shows a tilt of the stratopause. As the infrared emission of CO_2 molecules decreases with decreasing temperature, CO_2 may even have a net radiative warming effect in very cold atmospheric regions like the summer mesopause [*Schmidt et al.*, 2006]. Thus, the cooling effect of increasing CO_2 becomes smaller for lower temperatures.

[37] It should be noted that the future temperature trends depend on the expected development of stratospheric ozone which is prescribed to be the same in all RCPs. This is obviously not realistic as changes in the meridional circulation depend on the RCP (see below) and would lead to different ozone distributions. Differences between simulated temperature trends are hence exclusively caused by the radiative effect of changed CO_2 and adiabatic effects from changed circulation.

4.2. Dynamics

[38] Zonal winds in the middle atmosphere may either change as a response to changes in temperature caused by local radiative forcing, e.g., as a consequence of the development of the ozone hole, or as a response to changed momentum deposition from waves which may either be caused by changed wave generation or propagation [e.g., *Sigmond et al.*, 2004; *Schmidt et al.*, 2006; *McLandress and Shepherd*, 2009]. Changed momentum deposition affects also the meridional winds and subsequently, via downward control, the full circulation in the meridional plane.

[39] The middle column of Figure 11 shows the annual mean zonal wind changes in the past and the future. All trends have comparable features in most regions with significant signals. This particularly

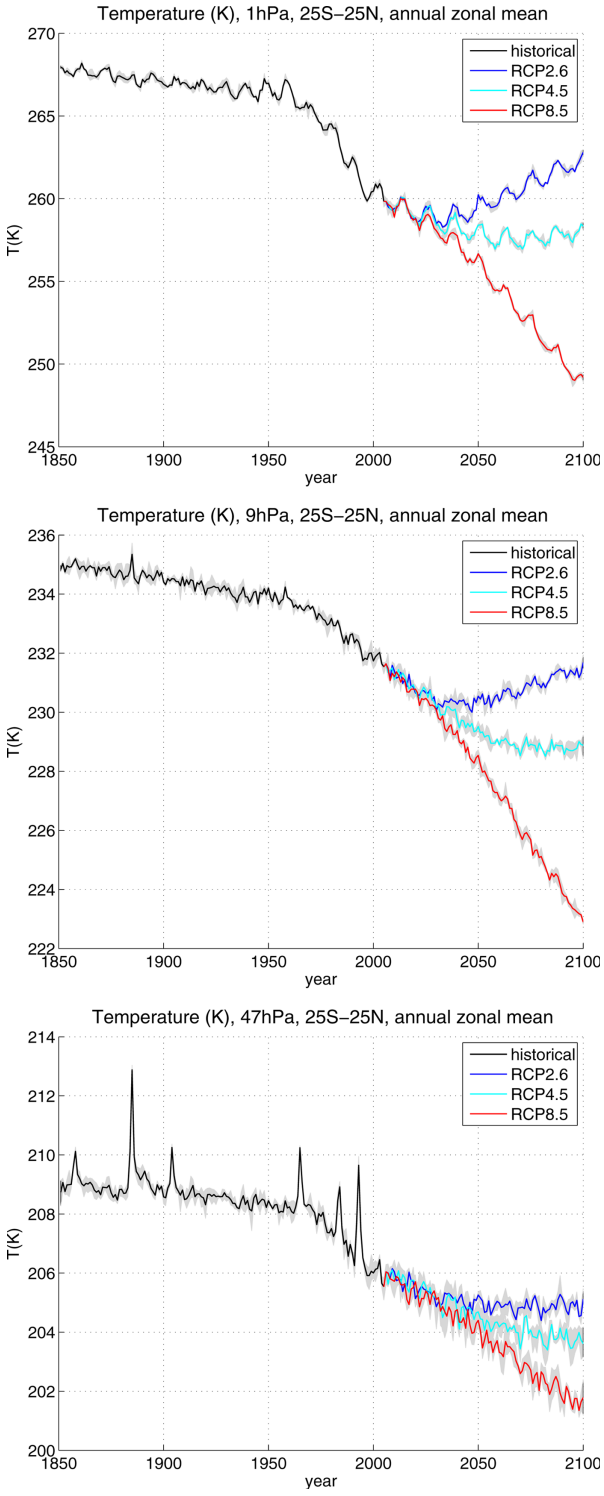

Figure 10. Time series of equatorial temperatures from the LR historical (black) and RCP simulations (RCP8.5: red, RCP4.5: cyan, RCP2.6: blue) for model layers centered at three different altitudes (top: 1 hPa, middle: 10 hPa, bottom: 47 hPa). Isolines give the averages of the three ensemble members; gray shading indicates the range spanned by maximum and minimum values of the three ensemble members.

concerns the well-known strengthening of subtropical tropopause jets which is caused by the increased latitudinal temperature gradient. Increasing westerlies are also simulated for the SH middle- to high-latitude stratosphere and mesosphere. By contrast, at the same northern latitudes trends are rather easterly. A particularly significant easterly response is caused by the strong forcing of RCP8.5. Figure 12 shows that the response of zonal mean zonal wind in DJF has a similar pattern as the annual response. The NH high-latitude annual mean easterly response in RCP8.5 is dominated by the DJF season. The dipole response of increasing westerlies at low and decreasing westerlies at high latitudes in boreal winter has been simulated previously by *Sigmond et al.* [2004] and is also a feature of the multimodel mean response in the CMIP5 1pctCO2 simulations, while the high-latitude easterly response was not characteristic in the mean CMIP3 response (Manzini et al., submitted manuscript, 2012). However, in ECHAM6-MR (not shown) the high internal variability of NH winter leads to insignificant high-latitude responses in most scenarios except for RCP8.5.

[40] The response of the meridional circulation, as represented by the mass stream function in the right column of Figures 11 and 12 indicates in most cases the well-known acceleration of the Brewer-Dobson circulation (BDC) that is related to increased wave drag in the extratropical stratosphere [e.g., *Butchart et al.*, 2006; *Garcia and Randel*, 2008; *McLandress and Shepherd*, 2009]. According to *Butchart et al.* [2010], however, the contributions of resolved and parameterized wave drag to the BDC changes vary substantially among models. For ECHAM5 this is discussed by *Karpechko and Manzini* [2012]. A more detailed analysis of the BDC response to increased GHG concentrations in ECHAM6 and its dependence on the model configuration is provided by *Bunzel and Schmidt* [2013].

5. Responses of the Middle Atmosphere to Natural Forcing

5.1. Multiple Linear Regression

[41] To quantify the influence of solar variability, stratospheric volcanic aerosols, and ENSO on the middle atmosphere we have performed a multiple linear regression (MLR) analysis for zonal mean temperature and zonal winds. For every altitude and latitude grid point, we adjust the parameters β_i of the following equation using a least squares regression to minimize the difference between the time series $Y(t)$ and the fitted model expressed with the residual error term $\varepsilon(t)$:

$$Y(t)=\overline{Y}+\beta_1 C_{CO_2}(t)+\beta_2\tau(t)+\beta_3 N_{3.4}(t)+\beta_4 I_{\mathrm{Hartley}}(t)+\beta_5\overline{u}_{28\mathrm{hPa}}(t)+\beta_6\overline{u}_{10\mathrm{hPa}}(t)+\epsilon(t), \quad (4)$$

where $C_{CO_2}(t)$ is the CO_2 mixing ratio, $\tau(t)$ is the globally averaged vertically integrated optical thickness of volcanic aerosol, $N_{3.4}(t)$ is the Niño3.4 index, $I_{\mathrm{Hartley}}(t)$

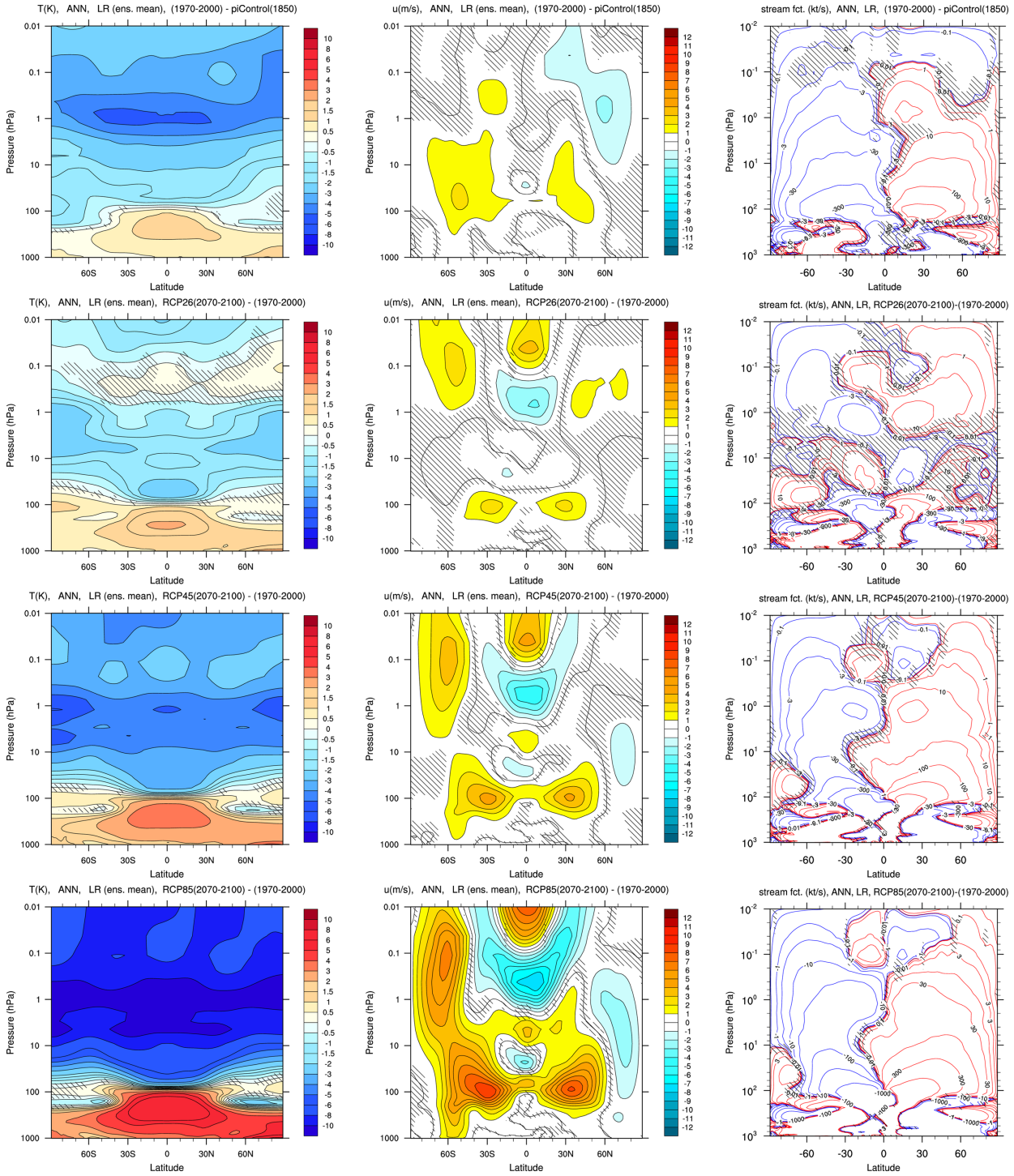

Figure 11. Annual and zonal mean changes in (left) temperature (K), (center) zonal wind (m/s), and (right) stream function (kt/s) simulated with the LR model. Changes are calculated between (top) the years 1970–2000 from the historical ensemble and 150 years of the preindustrial run, (2nd row) years 2070–2100 from the RCP2.6 ensemble and years 1970–2000 from the historical ensemble, (3rd row) as 2nd row but for RCP4.5, and (bottom) as 2nd row but for RCP8.5. Regions where the significance of the signals is below 95% are shaded.

is the solar irradiance in the spectral band of the RRTM scheme (120–263 nm) covering the Hartley band, and $\overline{u}_{28\mathrm{hPa}}$ and $\overline{u}_{10\mathrm{hPa}}$ are the simulated zonal mean zonal winds at 28 and 10 hPa, respectively. The zonal wind terms representing the QBO were only used for the MR model and not for the LR model that does not generate a QBO. It is interesting to note that the inclusion or exclusion of QBO terms in the regression of

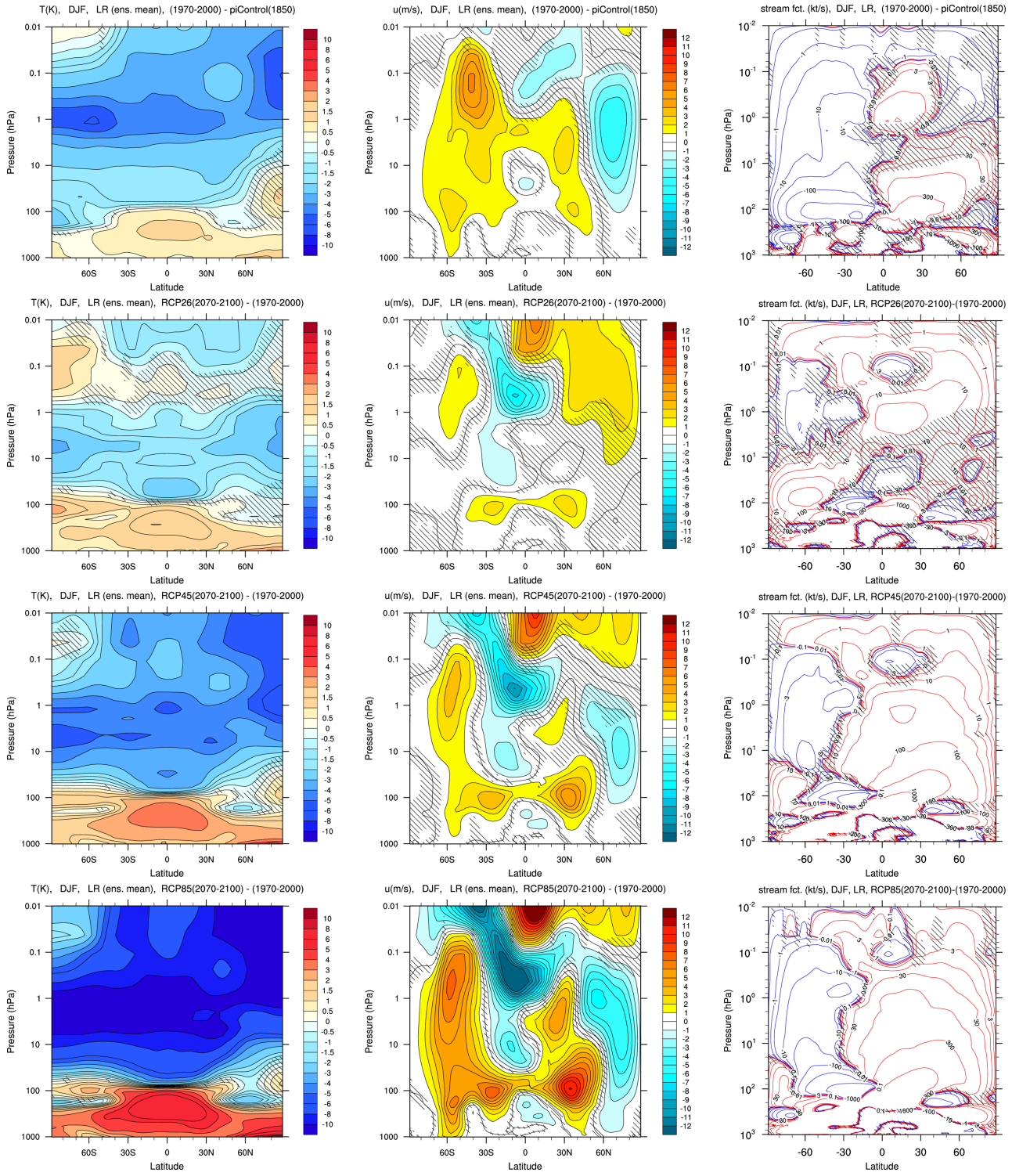

Figure 12. Same as Figure 11 but averaged over NH winter months (DJF).

MR results affects the results only very weakly. The length of the time series of three times 156 years apparently filters out possible aliasing effects from the QBO onto other forcings. To assess the annual mean responses, time series of deseasonalized monthly means were used, while the DJF responses were analyzed from time series of 3 month averages. We have used neither a lag term for the ENSO index nor an autoregression term. However, tests have been performed, and the results do not depend strongly on these choices. Results presented

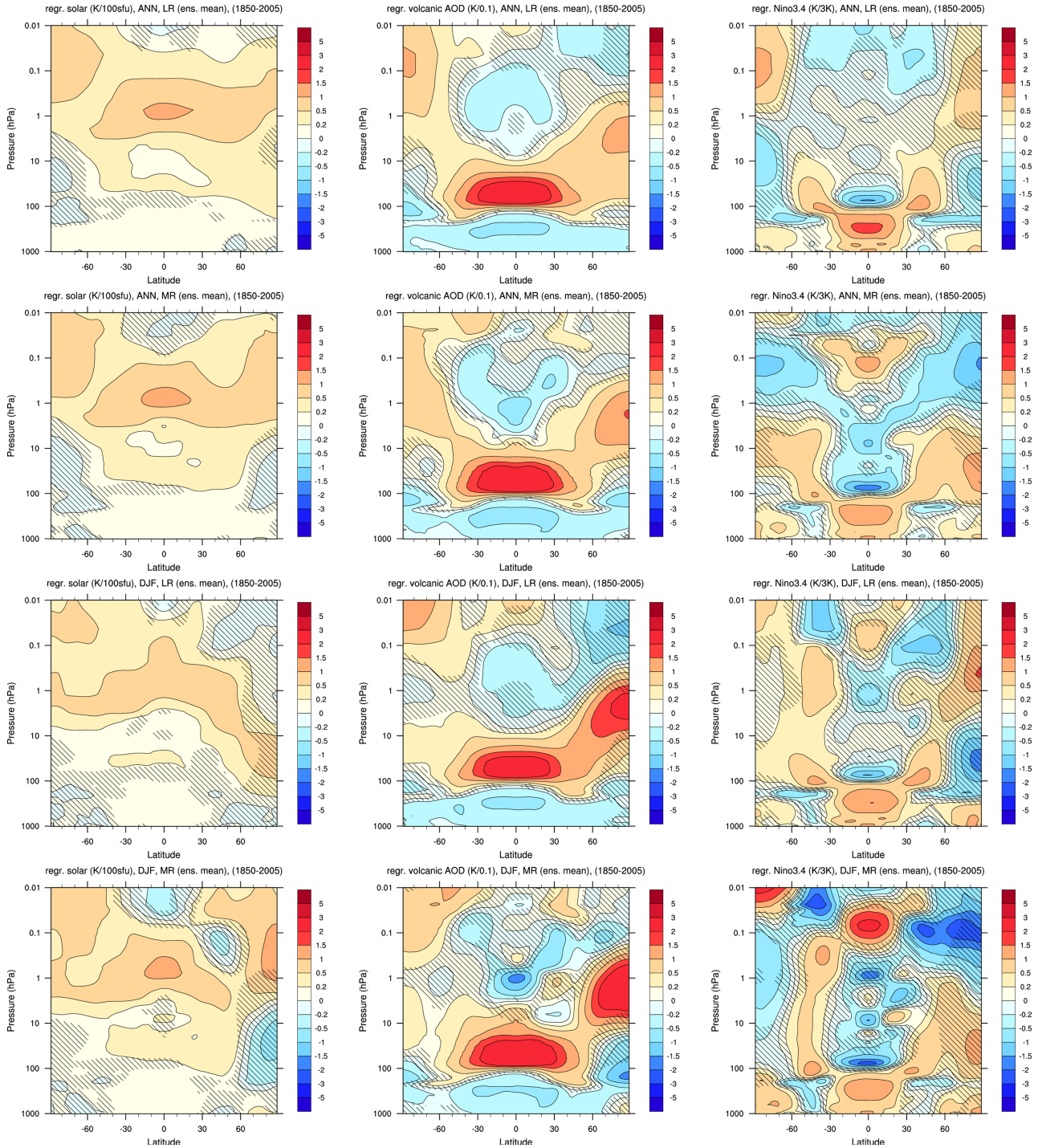

Figure 13. Regression coefficients obtained from (left) the regression of temperatures with respect to solar irradiance (K/100 sfu), (center) AOD of volcanic aerosols (K/0.1), and (right) units of the Nino3.4-ENSO index (K/3 K). Regressed was annual mean ensemble mean time series from the historical simulations with the (top) LR and (2nd row) MR models, and respective DJF means (3rd row: LR, bottom: MR). Regions where the significance of the signals is below 95% are shaded.

in the following were calculated from the ensemble mean time series of the historical simulations. However, performing an MLR independently for the three ensemble members and averaging the results gives similar results.

[42] Solar regression coefficients from the MLR in Figures 13 and 14 are expressed with respect to a change in solar irradiance corresponding to 100 solar flux units (sfu) of the 10.7 cm radio flux (F10.7). The

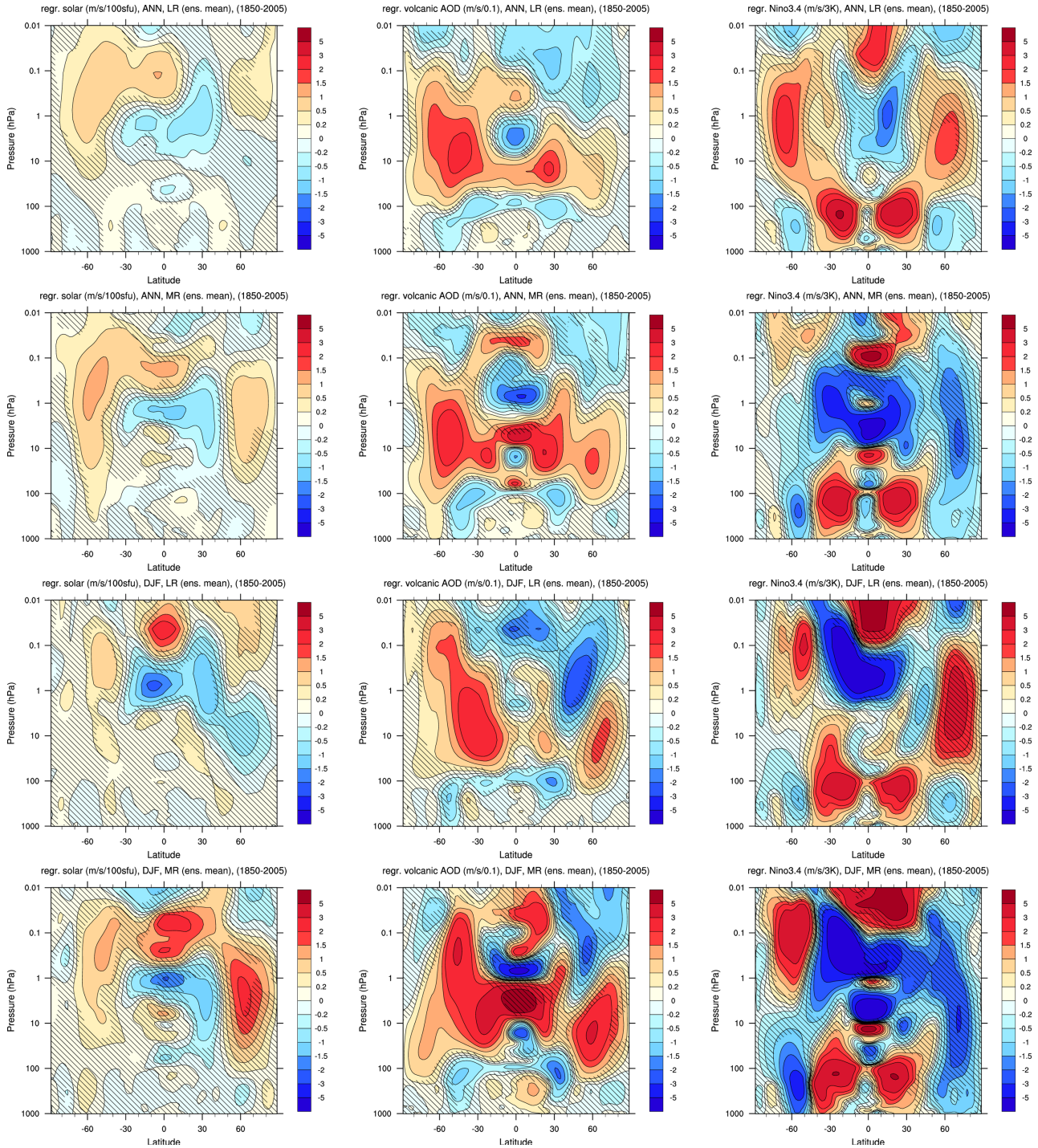

Figure 14. Same as Figure 13 but for zonal mean zonal winds (m/s).

MLR was performed with respect to the flux in the Hartley band but then scaled to 100 sfu using the very high correlation between F10.7 and Hartley band flux. Differences between typical solar maxima and minima are of about 130 sfu. The volcanic signals are expressed with respect to a global averaged optical depth (AOD) signal of 0.1. Figure 2 shows that this is a typical strength for a moderately strong volcanic eruption. ENSO signals are expressed with respect to a change of 3 K in the Nino3.4 index, which is a typical difference between moderate El Niño and La Niña peaks.

5.2. Temperature

[43] The time series of tropical temperatures in Figure 10 shows besides the trends also clear influences of the 11 year solar cycle (at 1 hPa) and of large volcanic eruptions (at 47 hPa). Results of the MLR for both DJF and annual means from both model configurations

show that the strongest solar signals of slightly more than 1 K/100 sfu appear in the tropical region close to the stratopause. This agrees well with an analysis of Stratospheric Sounding Unit satellite data by *Randel et al*. [2009a]. Another interesting feature is the secondary (although much weaker) maximum in the lower equatorial stratosphere. The origin and strength of such a secondary maximum are under discussion [e.g., *Gray et al*., 2010; *Matthes et al*., 2010; *Schmidt et al*., 2010]. An MLR of reanalysis data by *Frame and Gray* [2010] shows a much stronger secondary maximum than our simulations. However, it is also discussed to what extent this signal may be influenced from aliasing through ENSO [*Marsh and Garcia*, 2007]. High-latitude solar signals in temperature are in general of low statistical significance in our simulations.

[44] The temperature response to volcanic eruptions shows the typical pattern of a tropospheric cooling and a warming in the low- to middle-latitude lower stratosphere [e.g., *Robock*, 2000; *Timmreck*, 2012]. A consistent feature of MR and LR configurations is a significant warming in the NH winter high-latitude upper stratosphere.

[45] The ENSO signal in annual and DJF means for both configurations shows the expected warming in the tropical troposphere. The lower stratosphere is dominated by a strong cooling in the tropics and positive responses in middle latitudes. This pattern is known from earlier simulations and observations [*Randel et al*., 2009b]. Responses in the upper layers and high latitudes differ among the model configurations and are not significant in many areas. An exception are SH middle latitudes from the stratosphere to the lower mesosphere in DJF where a significant warming is simulated. The high-latitude NH response to ENSO in DJF is insignificant but of opposite sign in the LR and MR configurations. The warming simulated in MR would, however, fit better to the observed signal [e.g., *Manzini et al*., 2006].

5.3. Zonal Wind

[46] Zonal winds are related to the temperature patterns via the thermal wind relation. The latitudinal gradient of the temperature response to solar forcing in the upper stratosphere leads, hence, to westerly anomalies in the middle-latitude upper stratosphere and the lower mesosphere. The equatorial positive signal from volcanic forcing is reflected in the westerly anomalies in large parts of the stratospheric middle latitudes. In DJF this means an increase of the NH polar night jet, which is significant only in MR, and a decrease of the SH summer easterlies. In DJF a significant strengthening of the polar night is also simulated in response to volcanic forcing. However, a model intercomparison study by *Driscoll et al*. [2012] revealed that all of the participating CMIP5 models, including MPI-ESM-LR, underestimate the strong observed response of the NH winter stratosphere to a volcanic forcing [*Driscoll et al*., 2012]. It is interesting to note that the MR configuration simulates a stronger increase of the polar night jet (and stronger associated lower stratospheric polar cooling) which resembles more the observations than the signal simulated in MPI-ESM-LR. The response to ENSO is dominated by a strengthening of the subtropical tropopause jets. As in the case of temperatures, the comparison of signals in the two model configurations shows no consistent statistically significant patterns in large parts of the middle atmosphere. However, high-latitude responses in both temperature and wind would merit a further analysis with higher temporal resolution, as the signals are supposed to propagate during the course of the winter as discussed by *Kodera and Kuroda* [2002] for solar forcing and by *Cagnazzo and Manzini* [2009] for ENSO.

6. Summary and Conclusions

[47] ECHAM6 is the latest version of the series of ECHAM GCMs. Its uppermost layer is centered at 0.01 hPa (approximately 80 km), which makes it an appropriate tool for studies of the middle atmosphere and of vertical coupling processes. The goals of this paper were (a) to introduce those new features of ECHAM6 particularly relevant for the middle atmosphere, and the forcing data used in the CMIP5 simulations with the MPI-ESM, of which ECHAM6 is the atmospheric component and (b) to evaluate the simulated middle atmosphere and to describe the simulated response to natural and anthropogenic forcings.

[48] New features of ECHAM6 with respect to its predecessor ECHAM5 include (a) the short-wave radiation scheme RRTM-G that resolves the solar spectrum with now 14 instead of 4 or 6 bands and is hence better suited to study the impacts of solar variability, (b) the option to actually vary spectral irradiance independent of the variation of TSI, (c) the parameterization of methane oxidation as a source and of photodissociation as a sink of middle atmospheric water vapor, and (d) the option to use a latitude-dependent source strength for nonorographic gravity waves.

[49] For the CMIP5 simulations, data sets to account for external natural forcings had to be constructed. Special treatment was in particular required for atmospheric ozone. The ozone climatology recommended to be used in CMIP5 [*Cionni et al*., 2011] was extended upward, and a solar cycle variation was added to future ozone in order to allow for a consistent treatment of solar variability in past and future simulations.

[50] Simulated zonal average patterns of temperature and zonal wind are similar to those from ERA40 reanalyses. As expected, the variance of zonal mean quantities in the equatorial middle atmosphere is only well represented in the MR model configuration with high vertical resolution in the middle atmosphere that enables an internal generation of the QBO. A brief comparison of the QBO with observations shows that the QBO period is only realistically reproduced when the simulated atmosphere is forced by observed SSTs. One phenomenon that characterizes variability in high-latitude northern winter is the sudden stratospheric warming. The occurrence frequency of major warmings in ECHAM6 is only slightly larger than observed.

However, the seasonal distribution of warmings is not well reproduced by the model that produces too many warmings in early winter.

[51] Trends in model simulations have been calculated by comparing different simulated periods. As the model shows trends similar to observations in the relatively short period where such observations are available, we assume that the model is useful to estimate trends for the less recent past and the future. The future evolution of the middle atmosphere depends strongly on the emission scenario. Under the high emission scenario RCP8.5 some regions of the middle atmosphere are projected to be colder by about 20 K than during preindustrial times.

[52] The model response of the middle atmosphere to natural forcings as provided by solar variability, volcanic aerosols, and ENSO has been analyzed applying MLR technique. Many of the response patterns agree well with the observations. This is in particular true for the upper stratospheric temperature response to solar forcing that should benefit from the spectral resolution of the radiation code and from the prescribed ozone climatology.

[53] Differences between the atmospheric mean states and trends simulated with the LR and MR configurations are in general small except for the tropics where the QBO is a dominant feature. The high-latitude response in NH winter to volcanic and ENSO forcings seems to be simulated more realistically in the MR than in the LR model configuration. However, the statistical significance of these signals is low, and more simulations would be needed to test and understand the possible causes for these differences.

[54] The use of fixed trace gas climatologies in the studies of the response to natural and anthropogenic forcings should be mentioned as a caveat. In the real atmosphere, the distribution of ozone would respond to dynamical changes and feedback on them. Such feedbacks are excluded in our simulations.

[55] The large number of years simulated as part of the CMIP5 exercise with ECHAM6 and other models resolving at least the stratosphere permit studies of middle atmospheric dynamical phenomena based on the sound statistical samples. ECHAM6 results contribute, for example, to such intercomparison studies by *Charlton-Perez et al.* [2013], *Driscoll et al*. [2012], and Manzini et al. (submitted manuscript, 2012). While the focus of this paper was on providing an overview of the configuration of ECHAM6 as related to the processes relevant to the middle atmosphere, more detailed analyses of specific middle atmosphere features in ECHAM6 have already been performed [e.g., *Tomassini et al*., 2012; *Bunzel and Schmidt*, 2013] (Krismer et al., submitted manuscript, 2012) and will continue in the future.

[56] **Acknowledgments.** We like to thank Elisa Manzini for many useful comments and her contributions to the development of different middle atmosphere versions of ECHAM, and Bjorn Stevens for a careful internal review. Furthermore, we like to thank an anonymous reviewer for many helpful suggestions to improve this manuscript. We are grateful to Alexander Haumann for the preparation of Figure 4. Computational resources were made available and the CMIP5 simulations have been run by "Deutsches Klimarechenzentrum" (DKRZ) through support from the "Bundesministerium für Bildung und Forschung" (BMBF). F.B. acknowledges funding from the "Deutsche Forschungsgemeinschaft" (DFG) within the research group "SHARP" under grants GI 541/3-1 and SCHM 2158/2-2. C.T. acknowledges funding from the BMBF through the research program "MiKlip" (FKZ:01LP1130A).

References

Andrews, D. G., J. R. Holton, and C. B. Leovy (1987), *Middle Atmosphere Dynamics*, 489 pp., Academic, New York.

Baldwin, M. P., and T. J. Dunkerton (2001), Stratospheric harbingers of anomalous weather regimes, *Science*, *294*, 581–584, doi:10.1126/science.1063315.

Bancalá, S., K. Krüger, and M. Giorgetta (2012), The preconditioning of major sudden stratospheric warmings, *J. Geophys. Res.*, *117*, D04101, doi:10.1029/2011JD016769.

Bunzel, F., and F. Schmidt (2013), The Brewer-Dobson circulation in a changing climate: Impact of the model configuration, *J. Atmos. Sci.*, doi:10.1175/JAS-D-12-0215.1, in press.

Butchart, N., et al. (2006), Simulations of anthropogenic change in the strength of the Brewer-Dobson circulation, *Clim. Dyn.*, *27*, 727–741, doi:10.1007/s00382-006-0162-4.

Butchart, N., et al. (2010), Chemistry-climate model simulations of twenty-first century stratospheric climate and circulation changes, *J. Clim.*, *23*, 5349–5374, doi:10.1175/2010JCLI3404.1.

Cagnazzo, C., and E. Manzini (2009), Impact of the stratosphere on the winter tropospheric teleconnections between ENSO and the North Atlantic and European region, *J. Clim.*, *22*, 1223–1238, doi:10.1175/2008JCLI2549.1.

Cagnazzo, C., E. Manzini, M. A. Giorgetta, P. M. D. F. Forster, and J. J. Morcrette (2007), Impact of an improved shortwave radiation scheme in the MAECHAM5 general circulation model, *Atmos. Chem. Phys.*, *7*, 2503–2515.

Charlton, A. J., and L. M. Polvani (2007), A new look at stratospheric sudden warmings: Part I. Climatology and modeling benchmarks, *J. Clim.*, *20*, 449–469, doi:10.1175/JCLI3996.1.

Charlton, A. J., L. M. Polvani, J. Perlwitz, F. Sassi, E. Manzini, K. Shibata, S. Pawson, J. E. Nielsen, and D. Rind (2007), A new look at stratospheric sudden warmings: Part II. Evaluation of numerical model simulations, *J. Clim.*, *20*, 470–489, doi:10.1175/JCLI3994.1.

Charlton-Perz, A. J., et al. (2013), On the lack of stratospheric dynamical variability in low-top versions of the CMIP5 models, *J. Geophys. Res.*, doi:10.1002/jgrd.50125, in press.

Cionni, I., et al. (2011), Ozone database in support of CMIP5 simulations: results and corresponding radiative forcing, *Atmos. Chem. Phys.*, *11*, 11,267–11,292, doi:10.5194/acp-11-11267-2011.

Driscoll, S., A. Bozzo, L. J. Gray, A. Robock, and G. Stenchikov (2012), Coupled Model Intercomparison Project 5 (CMIP5) simulations of climate following volcanic eruptions, *J. Geophys. Res.*, *117*, D17105, doi:10.1029/2012JD017607.

Eyring, V., et al. (2010), Multi-model assessment of stratospheric ozone return dates and ozone recovery in CCMVal-2 models, *Atmos. Chem. Phys.*, *10*, 9451–9472, doi:10.5194/acp-10-9451-2010.

Farman, J. C., B. G. Gardiner, and J. D. Shanklin (1985), Large losses of total ozone in Antarctica reveal seasonal ClO_x/NO_x interaction, *Nature*, *315*, 207–210, doi:10.1038/315207a0.

Fouquart, Y., and B. Bonnel (1980), Computations of solar heating of the earth's atmosphere: A new parameterization, *Contrib. Atmos. Phys.*, *53*, 35–62.

Frame, T. H. A., and L. J. Gray (2010), The 11-year solar cycle in ERA-40 data: An update to 2008, *J. Clim.*, *23*, 2213–2222, doi:10.1175/2009JCLI3150.1.

Froehlich, C. (2004), Solar irradiance variability, in *Solar Variability and Its Effects on Climate, Geophys. Monogr. Ser.*, vol. *141*, edited by J. M. Pap and P. Fox, pp. 97–110, AGU, Washington, D. C.

Garcia, R. R., and W. J. Randel (2008), Acceleration of the Brewer-Dobson circulation due to increases in greenhouse gases, *J. Atmos. Sci.*, *65*, 2731–2739, doi:10.1175/2008JAS2712.1.

Giorgetta, M. A., E. Manzini, and E. Roeckner (2002), Forcing of the quasi-biennial oscillation from a broad spectrum of atmospheric waves, *Geophys. Res. Lett.*, *29*, doi:10.1029/2002GL014756.

Giorgetta, M. A., E. Manzini, E. Roeckner, M. Esch, and L. Bengtsson (2006), Climatology and forcing of the quasi-biennial oscillation in the MAECHAM5 model, *J. Clim.*, *19*, 3882–3901, doi:10.1175/JCLI3830.1.

Gray, L. J., et al. (2010), Solar influences on climate, *Rev. Geophys.*, *48*, RG4001, doi:10.1029/2009RG000282.

Hines, C. O. (1997a), Doppler-spread parameterization of gravity wave momentum deposition in the middle atmosphere: Part 1. Basic formulation, *J. Atmos. Sol. Terr. Phys.*, *59*, 371–386.

Hines, C. O. (1997b), Doppler-spread parameterization of gravity wave momentum deposition in the middle atmosphere: Part 2. Broad and quasi monochromatic spectra, and implementation, *J. Atmos. Sol. Terr. Phys.*, *59*, 387–400.

Karpechko, A. Y., and E. Manzini (2012), Stratospheric influence on tropospheric climate change in the northern hemisphere, *J. Geophys. Res.*, *117*, D05133, doi:10.1029/2011JD017036.

Kawatani, Y., K. Hamilton, and A. Noda (2012), The effects of changes in sea surface temperature and CO_2 concentration on the quasi-biennial oscillation, *J. Atmos. Sci.*, *69*, 1734–1749, doi:10.1175/JAS-D-11-0265.1.

Kodera, K., and Y. Kuroda (2002), Dynamical response to the solar cycle, *J. Geophys. Res.*, *107*(D24), 4749, doi:10.1029/2002JD002224.

Langematz, U., M. Kunze, K. Krüger, K. Labitzke, and G. L. Roff (2003), Thermal and dynamical changes of the stratosphere since 1979 and their link to ozone and CO_2 changes, *J. Geophys. Res.*, *108*, 4027, doi:10.1029/2002JD002069.

Lean, J. (2000), Evolution of the Sun's spectral irradiance since the Maunder minimum, *Geophys. Res. Lett.*, *27*, 2425–2428.

Lott, F., and M. J. Miller (1997), A new subgrid-scale orographic drag parameterization: Its formulation and testing, *Q. J. R. Meteorol. Soc.*, *123*, 101–127.

Manzini, E., and N. A. McFarlane (1998), The effect of varying the source spectrum of a gravity wave parameterization in a middle atmosphere general circulation model, *J. Geophys. Res.*, *103*, 31,523–31,540, doi:10.1029/98JD02274.

Manzini, E., N. A. McFarlane, and C. McLandress (1997), Impact of the Doppler spread parameterization on the simulation of the middle atmosphere circulation using the MA/ECHAM4 general circulation model, *J. Geophys. Res.*, *102*, 25,751–25,762.

Manzini, E., M. A. Giorgetta, M. Esch, L. Kornblueh, and E. Roeckner (2006), The influence of sea surface temperatures on the northern winter stratosphere: Ensemble simulations with the MAECHAM5 model, *J. Clim.*, *19*(16), 3863–3881.

Marsh, D. R., and R. R. Garcia (2007), Attribution of decadal variability in lower-stratospheric tropical ozone, *Geophys. Res. Lett.*, *34*, L21807, doi:10.1029/2007GL030935.

Matthes, K., D. R. Marsh, R. R. Garcia, D. E. Kinnison, F. Sassi, and S. Walters (2010), Role of the QBO in modulating the influence of the 11 year solar cycle on the atmosphere using constant forcings, *J. Geophys. Res.*, *115(D14)*, D18110, doi:10.1029/2009JD013020.

Mauritsen, T., et al. (2012), Tuning the climate of a global model, *J. Adv. Model. Earth Syst.*, *4*, M00A01, doi:10.1029/2012MS000154.

McLandress, C., and T. G. Shepherd (2009), Simulated anthropogenic changes in the Brewer-Dobson circulation, including its extension to high latitudes, *J. Clim.*, *22*, 1516, doi:10.1175/2008JCLI2679.1.

Meehl, G. A., C. Covey, T. Delworth, M. Latif, B. McAvaney, J. F. B. Mitchell, R. J. Stouffer, and K. E. Taylor (2007), THE WCRP CMIP3 multimodel dataset: A new era in climate change research, *Bull. Am. Meteorol. Soc.*, *88*, 1383–1394, doi:10.1175/BAMS-88-9-1383.

Mlawer, E. J., S. J. Taubman, P. D. Brown, M. J. Iacono, and S. J. Clough (1998), Shortwave and longwave enhancements in the rapid radiative transfer model, paper presented at the 7th Atmospheric Radiation Measurement (ARM) Science Team Meeting, CONF-970365, U.S. Dep. of Energy, Washington, D. C.

Randel, W. J., et al. (2009a), An update of observed stratospheric temperature trends, *J. Geophys. Res.*, *114(D13)*, D02107, doi:10.1029/2008JD010421.

Randel, W. J., R. R. Garcia, N. Calvo, and D. Marsh (2009b), ENSO influence on zonal mean temperature and ozone in the tropical lower stratosphere, *Geophys. Res. Lett.*, *36*, L15822, doi:10.1029/2009GL039343.

Robock, A. (2000), Volcanic eruptions and climate, *Rev. Geophys.*, *38*, 191–220, doi:10.1029/1998RG000054.

Roeckner, E., et al. (2003), The atmospheric general circulation model ECHAM 5: Part I. Model description, Tech. Rep. 349, MPI for Meteorol., Hamburg, Germany.

Roeckner, E., R. Brokopf, M. Esch, M. Giorgetta, S. Hagemann, L. Kornblueh, E. Manzini, U. Schlese, and U. Schulzweida (2006), Sensitivity of simulated climate to horizontal and vertical resolution in the ECHAM5 atmosphere model, *J. Clim.*, *19*, 3771–3791.

Scaife, A. A., J. R. Knight, G. K. Vallis, and C. K. Folland (2005), A stratospheric influence on the winter NAO and North Atlantic surface climate, *Geophys. Res. Lett.*, *32*, L18715, doi:10.1029/2005GL023226.

Schmidt, H., et al. (2006), The HAMMONIA chemistry climate model: Sensitivity of the mesopause region to the 11-year solar cycle and CO_2 doubling, *J. Clim.*, *19*(16), 3903–3931.

Schmidt, H., G. P. Brasseur, and M. A. Giorgetta (2010), Solar cycle signal in a general circulation and chemistry model with internally generated quasi-biennial oscillation, *J. Geophys. Res.*, *115*(D14), D00I14, doi:10.1029/2009JD012542.

Sigmond, M., P. C. Siegmund, E. Manzini, and H. Kelder (2004), A simulation of the separate climate effects of middle-atmospheric and tropospheric CO_2 doubling., *J. Clim.*, *17*, 2352–2367, doi:10.1175/1520-0442.

Stenchikov, G., K. Hamilton, A. Robock, V. Ramaswamy, and M. D. Schwarzkopf (2004), Arctic oscillation response to the 1991 Pinatubo eruption in the SKYHI general circulation model with a realistic quasi-biennial oscillation, *J. Geophys. Res.*, *109*(D18), D03112, doi:10.1029/2003JD003699.

Stenchikov, G., K. Hamilton, R. J. Stouffer, A. Robock, V. Ramaswamy, B. Santer, and H.-F. Graf (2006), Arctic oscillation response to volcanic eruptions in the IPCC AR4 climate models, *J. Geophys. Res.*, *111*(D10), D07107, doi:10.1029/2005JD006286.

Stenchikov, G. L., I. Kirchner, A. Robock, H.-F. Graf, J. C. Antuña, R. G. Grainger, A. Lambert, and L. Thomason (1998), Radiative forcing from the 1991 Mount Pinatubo volcanic eruption, *J. Geophys. Res.*, *103*, 13,837–13,858, doi:10.1029/98JD00693.

Stevens, B., et al. (2013), The atmospheric component of the MPI?M earth system model: ECHAM6, *J. Adv. Model. Earth Syst.*, in press.

Taylor, K. E., R. J. Stouffer, and G. A. Meehl (2012), An overview of CMIP5 and the experiment design, *Bull. Am. Meteorol. Soc.*, *93*, 485–498, doi:10.1175/BAMS-D-11-00094.1.

Thomas, M. A., C. Timmreck, M. A. Giorgetta, H.-F. Graf, and G. Stenchikov (2009), Simulation of the climate impact of Mt. Pinatubo eruption using ECHAM5: Part 1. Sensitivity to the modes of atmospheric circulation and boundary conditions, *Atmos. Chem. Phys.*, *9*, 757–769.

Thompson, D. W. J., and S. Solomon (2002), Interpretation of recent southern hemisphere climate change, *Science*, *296*, 895–899, doi:10.1126/science.1069270.

Timmreck, C. (2012), Modeling the climatic effects of large explosive volcanic eruptions, *Wiley Interdiscip. Rev. Clim. Change*, *3*, 545–564, doi:10.1002/wcc.192.

Tomassini, L., E. P. Gerber, F. Bunzel, and M. Giorgetta (2012), The role of stratosphere-troposphere coupling in the occurrence of extreme winter cold spells over northern Europe, *J. Adv. Model. Earth Syst.*, *4*, M00A03, doi:1029/2012MS000177.

Corresponding author: H. Schmidt, Max Planck Institute for Meteorology, Bundesstr. 53, D-20146 Hamburg, Germany. (hauke.schmidt@zmaw.de)